*Metrol. Meas. Syst.*, Vol. XX (2013), No. 2, pp. 159–170.

PAN POLSKA AKADEMIA NAUK

METROLOGY AND MEASUREMENT SYSTEMS

Index 330930, ISSN 0860-8229

*www.metrology.pg.gda.pl*

M&MS

# Modeling of HgCdTe LWIR detector for high operation temperature conditions

**P. Martyniuk[1)], W. Gawron[1)], P. Madejczyk[1)], A. Rogalski[1)], J. Piotrowski[2)]**

*1)Institute of Applied Physics, Military University of Technology, 2 Kaliskiego Str., 00-908 Warsaw, Poland (✉ pmartyniuk@wat.edu.pl, +48 22 6839673)*

*2)Vigo System S.A., 129/133 Poznańska Str., 05-850 Ożarów Mazowiecki, Poland (wgawron@wat.edu.pl, +48 22 6839673)*

**Abstract**

The paper reports on the photoelectrical performance of the long wavelength infrared (LWIR) HgCdTe high operating temperature (HOT) detector. The detector structure was simulated with commercially available software APSYS by Crosslight Inc. taking into account SRH, Auger and tunnelling currents. A detailed analysis of the detector performance such as dark current, detectivity, time response as a function of device architecture and applied bias is performed, pointing out optimal working conditions.

Keywords: HgCdTe, IR detector, Auger suppression, HOT detectors.



## 1. Introduction

Long-wave infrared photodetectors are important in a variety of applications. The key condition which must be fulfilled to design the high operation temperature (HOT) detector is to achieve a low dark current produced mostly by the Shockley-Read-Hall (SRH) generation-recombination (G-R) process, Auger G-R and both band-to-band (BTB)/trap-assisted-tunnelling (TAT) mechanisms [1–4].

The long-wave infrared radiation's (LWIR) detection at near-ambient temperatures has been discussed in many papers and reviewed in the recently published monographs [5–6]. The first uncooled 10.6 μm photodetectors based on epitaxial graded gap structures were demonstrated in 1972 [7–8]. Further development of the uncooled detectors relied on the three-dimensional concept of the devices [9], based on integration of the optical and detection function in a monolithic heterostructure chip. In practice, most of infrared device-photoconductors, photoelectromagnetic, and especially photodiodes are based on heterostructures to prevent parasitic thermal generation at contacts, surfaces and interfaces. In addition, the heterostructure design reduces parasitic impedances, and improves responsivity and frequency response. In the solution proposed by British scientists, the $N^+đP^+$ architecture was used [10], in which extraction and exclusion of thermally generated charge carriers from the active region under reverse bias was applied. Initially, three layer $N^+đP^+$ structures were used, where đ denotes the absorber region with extrinsic doping lower in comparison with intrinsic concentration. Complex three-, four- and five-layer structures were used with great success for LWIR photodiodes operating at near-room temperatures [11–13]. Polish scientists improved photodetectors based on epitaxial graded gap structures [14–19]. Paper [20]

Article history: received on Apr. 02, 2013; accepted on May. 27, 2013; available online on Jun. 03, 2013; DOI: 10.2478/mms-2013-0014.

presents recent results on design, fabrication and properties of photodiodes with graded interfaces, operating at near-room temperatures. The main modification in comparison with the standard three – layer $N^+pP^+$ structure is programmed grading of band gap and doping level at interfaces. Such HgCdTe detector conception, in which the transport of majority and minority carriers is determined by barriers and Auger G-R suppression, has been used with great success for the HOT conditions.

At present, the structures in which the transport of majority and minority carriers is determined by barriers are called barrier IR detectors (BIRDs). Recently, $A^{III}B^{V}$ family compounds, including type II superlattices (T2SLs), emerged to play a dominant role in the designing of the unipolar barrier infrared detectors (UBIRD) due to a nearly zero band-offset in the valance band [21–23]. Although the fundamental physical properties of T2SLs' indicate their potential superiority over bulk materials, we have predicted that similarly to the technological problems related to the growth of self-organized quantum dot infrared photodetectors (QDIPs), InAs/GaSb T2SLs' development is limited by technological problems connected with the growth of uniform and thick enough SLs [24–25]. What is more, short minority carrier lifetimes ($\tau_{DIF}$, $\tau_{GR}$ < 10 ns in the temperature range > 200 K) also impede the development of the T2SLs IR devices [26–28].

In a different solution proposed by Polish scientists, the structures based on multiple heterojunctions have been used for long-wave infrared detectors operating at room temperature [29–32].

In this paper we present the concept of a photodetector based on epitaxial graded gap structures [33–36]. Figure 1 shows the structure of the photodiode in which a narrow-gap absorber is sandwiched between wider gap minority and majority carrier contacts. The main layers are interfaced with thin graded gap and doping level transition layer that are formed by diffusion processes during growth of the nominally layer structure or introduced with programmed growth. The device is illuminated through the $N^+$ layer which plays a role of an infrared transmitting window for photons with energies below the band gap. Since diffusion length in the $N^+$ layer is short compared to its thickness, the charge carriers generated in the layer do not produce a photocurrent so the band gap of the layer determines the cut-off wavelength of the device.

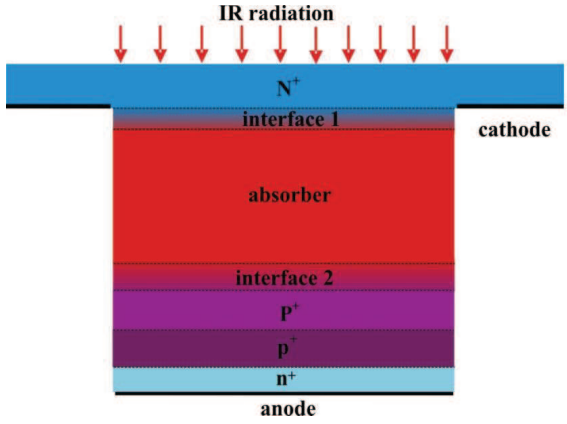


Fig. 1. Schematic structure of heterojunction diode with graded interfaces.

We simulated this HgCdTe detector concept, in which the transport of majority and minority carriers is determined by barriers and Auger G-R suppression, as a solution for the HOT conditions. We present the performance of the LWIR HgCdTe detector with extra Auger G-R suppression and

cut-off wavelength of $\lambda_c$ = 8.3 μm at $T$ = 300 K. The voltage and structural dependences of the dark current, detectivity are analyzed including both TAT and BTB processes at the heterojunctions

## 2. Simulation procedure and experimental results

Table 1 shows parameters taken in modelling of LWIR $N^+/N/P1/\pi/P2/P^+/p^+/n^+$ type detectors. P1 and P2 interface layers were assumed to be *x*-graded regions and represent the real structure whose profile is shaped by interdiffusion processes during $Hg_{1-x}Cd_xTe$ growth. The doping profiles were modelled by applying Gauss tail model (the dopant concentration falls off with a Gaussian tail on the edges of the polygon; *dx* [37]; see Table 1). The $p^+$-$n^+$ junction has been applied for improvement of electrical contact property between the $P^+$ region and metallization.

Table 1. Parameters taken in modeling of LWIR $N^+/N/P1/\pi/P2/P^+/p^+/n^+$ type detectors

| | $N^+$ | N | P1 | π-Absorber | P2 | $P^+$ | $p^+$ | $n^+$ |
|---|---|---|---|---|---|---|---|---|
| $N_A$, $N_D$ [$cm^{-3}$] | $10^{18}$ | $10^{16}$ | $8\times10^{15}$ | $8\times10^{15}$ | $5\times10^{17}$ | $5\times10^{17}$ | $5\times10^{17}$ | $10^{18}$ |
| Gauss tail, *dx* [μm] | 0.05 | 0.05 | 0.1 | 0.1 | 0.1 | 0.05 | 0.02 | 0.02 |
| Composition, *x* | 0.48 | 0.19→0.48 | 0.19→0.48 | 0.19 | 0.2→0.48 | 0.2→0.48 | 0.2→0.48 | 0.2→0.48 |
| Geometry, *d* [μm] | 9 | 0.8 | 0.4 | 5.4 | 1 | 2 | 2 | 1.5 |
| $A$ [$\mu m^2$] | Electrical area | | | | 100×75 | | | |
| $T_s$, , $\theta$ | Background temperature, field of view | | | | 300 K, 20° ($f_\#$=2.835) | | | |
| $F_1F_2$ | Overlap matrix | | | | 0.21 | | | |
| $E_{Trap}$ | Trap energy level | | | | $0.25\times E_g$ | | | |
| $N_{Trap}$ [$cm^{-3}$] | Trap concentration | | | | $5\times10^{14}$ | | | |
| SHR/TAT, $\tau_n$, $\tau_p$ [ns] | Minority carrier lifetime | | | | 40, 11 | | | |
| $\Phi$ [$W/m^2$] | Incident power density | | | | 500 | | | |

Theoretical modeling of the HgCdTe heterostructures has been performed by numerical solving of Poisson's equation and the electron/hole current continuity equations with the use of the commercially available APSYS platform (Crosslight Inc.). APSYS uses the Newton-Richardson method of nonlinear iterations. The applied model incorporates both HgCdTe electrical and optical properties to estimate limiting device's performance by taking into account the influence of radiative (RAD), Auger (AUG), SRH G-R and BTB as well as TAT tunnelling mechanisms. The HgCdTe absorption coefficient was estimated according to nonparabolic Kane model including its composition and temperature dependences. Computations were performed using the Fermi-Dirac statistics for a nondegenerate semiconductor model with parabolic energy bands. The specific equations describing steady-state drift-diffusion (D-D) model and HgCdTe parameters used in calculation of recombination rates are described in details in Capper's monograph, APSYS manual and previous Martyniuk's *et al*. papers [37–40].

The noise current was simulated using the expression including the thermal Johnson-Nyquist component, optical and electrical shot contributions:

$$i_n(V) = \sqrt{4k_BT/RA + 2qI_B 2qJ_{DARK}}\ , \tag{1}$$

where $A$ is the detector's area, $RA$ dynamic resistance area product, $I_{DARK}$ and $I_B$ are the dark current density and background induced current, respectively, and $k_B$ is Boltzmann constant.

The quantum efficiency is a function of the incident radiation wavelength and current responsivity, $R_i$, (without electro-optical gain) while detectivity is defined by the following expressions:

$$\eta(\lambda) = 1.24\frac{R_i}{\lambda}, \qquad D^* = \frac{R_i}{i_n(V)}\sqrt{A}\ . \tag{2}$$

The $N^+/N/P1/\pi/P2/P^+/p^+/n^+$ structure with absorber composition of $x = 0.19$, its thickness of $t = 5.4$ μm, and $p$-type doping ($N_A = 8\times10^{15}$ cm$^{-3}$) is shown in Fig. 2. The secondary ion mass spectroscopy (SIMS) measurements were used to verify the compositional and doping profiles of the simulated structure. SIMS profiles shown in Fig. 3 fully confirm the assumed growth procedure.

The devices presented in this paper were fabricated in a joint laboratory run by VIGO System S.A. and Military University of Technology (MUT). The (111) HgCdTe epiready layers were grown on 2" inch semi-insulating (100) GaAs substrates in a horizontal MOCVD AIX 200 reactor. The interdiffused multilayer process (IMP) technique was applied for the HgCdTe layers deposition. A detailed description of the MOCVD growth procedure is presented in Ref. [41–42].

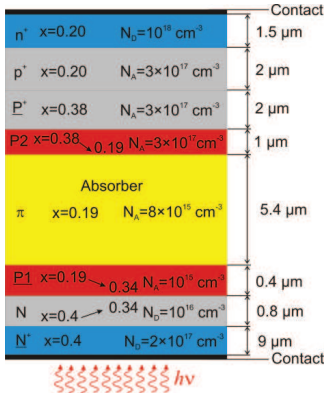


Fig. 2. Simulated $N^+/N/P1/\pi/P2/P^+/p^+/n^+$ HgCdTe heterostructure.

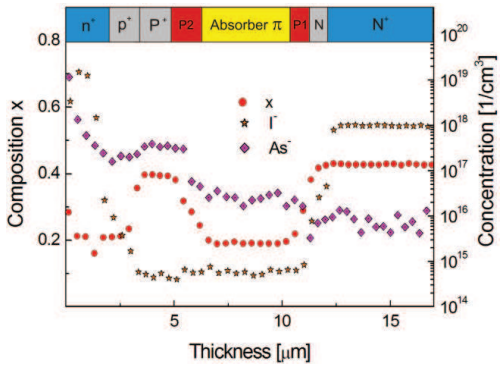


Fig. 3. SIMS profile of the HgCdTe heterostructure.

The measured and simulated spectral response characteristics for $V = -400$ mV are presented in Fig. 4. The 50 % cut-off wavelength assumes $\lambda_c = 8.3$ μm at $T = 300$ K. The maximum responsivity of $R_i \approx 3$ A/W is estimated for $\lambda = 6.75$ μm. Three heterojunctions, $N^+$-π (extraction), π-$P^+$ (exclusion) and $p^+$-$n^+$ (for improvement of electrical contact) with $x$-graded sub-layers, were found to play a dominant role in performance modeling of the mentioned structure. The absorption of IR radiation occurs only in the π-type absorber and its dependence on wavelength for $x = 0.19$ an $T = 300$ K is presented in Fig. 4 (dashed line).

The measured and simulated $J_{DARK}$ characteristics are presented in Fig. 5. The simulation includes RAD, AUG, SRH and TAT/BTB contributions. The trap density, $N_t$, and trap energy level, $E_t$, were assumed at $N_t = 5\times10^{14}$ cm$^{-3}$ and $E_t = 0.25E_g$, respectively (counted from the conduction band). The series resistance influences the slope of the $J$-$V$ characteristics and was found to be at the level of $R_{Series} = 14$ Ω. The detector structure area was estimated as $A = 7.9\times10^{-9}$ m$^2$. The characteristic SRH and TAT lifetimes were assumed to be at the same level: $\tau_n = 40$ ns and $\tau_p = 11$ ns, respectively. As the reverse-biased $J$-$V$ characteristics is concerned, a rapid increase of $J_{DARK}$ is observed to $V_{Max} = -150$ mV. In this voltage region the differential resistance increases and at the final stage becomes infinite. Once the applied voltage increases, the minimum $J_{DARK}$ is reached at a reverse bias of $V_{Min} = -220$ mV and the $J$-$V$ characteristics exhibits a negative differential resistance (NDR as a result of AUG G-R suppression). The SRH G-R and the tunnelling mechanism contribute to the net dark current for voltage $V = V_{Min}$. Further increase of the reverse voltage ($V > -220$ mV) leads to an increase of the $J_{DARK}$ due to tunnelling effects at the decisive heterojunctions (especially TAT).

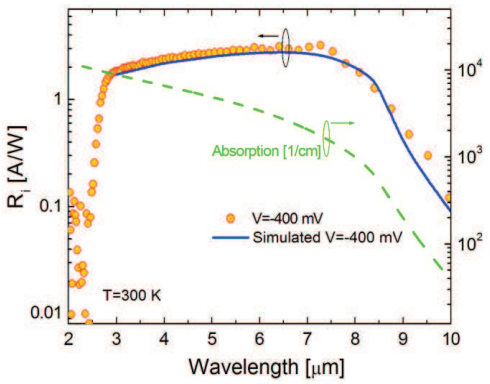


Fig. 4. Spectral response of LWIR $N^+/N/P1/\pi/P2/P^+/p^+/n^+$ HgCdTe structure.

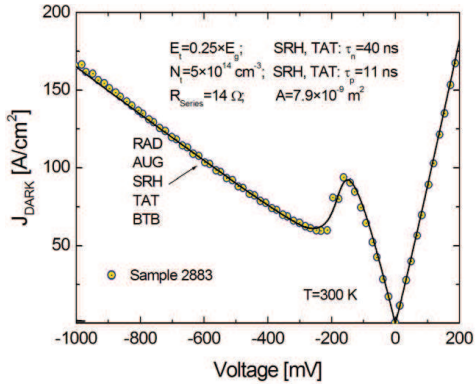


Fig. 5. Measured and modeled dark current density of LWIR $N^+/N/P1/\pi/P2/P^+/p^+/n^+$ HgCdTe structure.

## 3. Results and discussion

### 3.1. Band diagrams

The modeled energy band diagram profile of the LWIR structure is presented in Fig. 6. The calculations were performed for HOT conditions, $T$ = 300 K, using zero and the reverse bias voltage polarizations ($V$ = –400 mV). Under reverse voltage polarization, the electrons are extracted from the absorber region by the positive electrode connected to the $N^+$-contact layer ($N^+$-π heterojunction). The electrons are also excluded from the absorber near the π-$P^+$ junction because they cannot be injected from the negative electrode into the $P^+$-layer. The energy barrier between the $n^+$ and $P^+$ regions enhance exclusion of electrons from the absorber region and, as a consequence, they cannot be replenished due to the low concentration of electrons in the $P^+$-barrier region.

(a) (b)

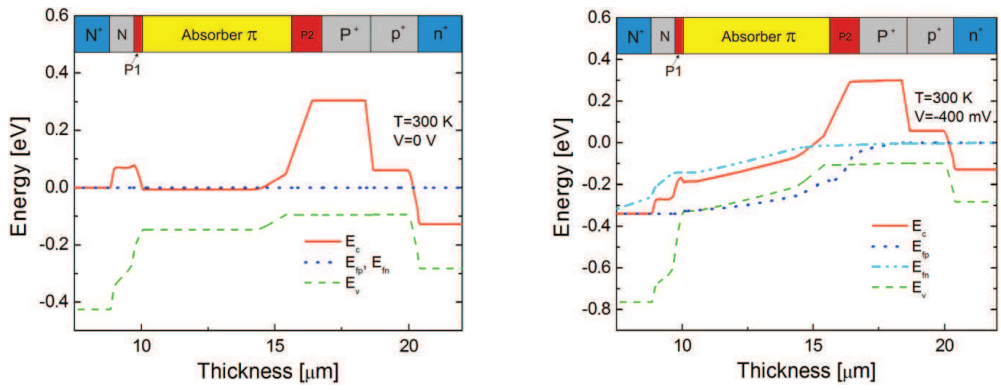


Fig. 6. Energy band diagram of LWIR $N^+/N/P1/\pi/P2/P^+/p^+/n^+$ HgCdTe structure: (a) at equilibrium, (b) at reverse bias $V$ = – 400 mV.

### 3.2. Dark current simulation

As mentioned above, three heterojunctions contribute to the net current as TAT and BTB mechanisms are concerned. The influence of individual heterojunctions on dark current characteristics is depicted in Fig. 7. The level of AUG G-R suppression may be easily estimated by the difference between $J_{Max}$ and $J_{Min}$. The black line shows RAD, AUG and SRH's contribution in the net dark current. NDR due to AUG G-R suppression is observable for $V > -200$ mV ($J_{Max} - J_{Min}$ = 13.2 A/cm$^2$). The red dashed line presents RAD, AUG, SRH and extra BTB/TAT contribution at the $N^+$-π extraction heterojunction. The AUG G-R suppression is limited and the NDR region is barely visible ($J_{Max} - J_{Min}$ = 2.3 A/cm$^2$). BTB/TAT mechanism shapes the $J_{DARK}$ characteristics for $V > -350$ mV. Influence of the tunnelling mechanism at the exclusion π-$P^+$ heterojunction is shown by the green dotted line. The level of AUG G-R suppression given by the $J_{Max} - J_{Min}$ difference reaches the maximum value of 39.19 A/cm$^2$. The influence of BTB/TAT processes at the $p^+$-$n^+$ junction (which improves electrical contact properties between the $P^+$ region and metallization) on $J_{DARK}$ is depicted by the blue dashed-dotted line. The analyzed $p^+$-$n^+$ junction is forward biased and the tunnelling mechanism dominates at lower voltages in comparison to the RAD, AUG, and SRH contributions ($J_{Max} - J_{Min}$ = 11.2 A/cm$^2$). The reduction of both the BTB and TAT mechanisms at the extraction $N^+$-π heterojunction and reinforcement of tunnelling effects at $p^+$-$n^+$ heterojuction should reduce the dark current (e.g. for $V = -400$ mV three times and for $V = -1000$ mV six times, respectively). Similar results could be obtained by proper optimization of the π-$P^+$ exclusion heterojunction.

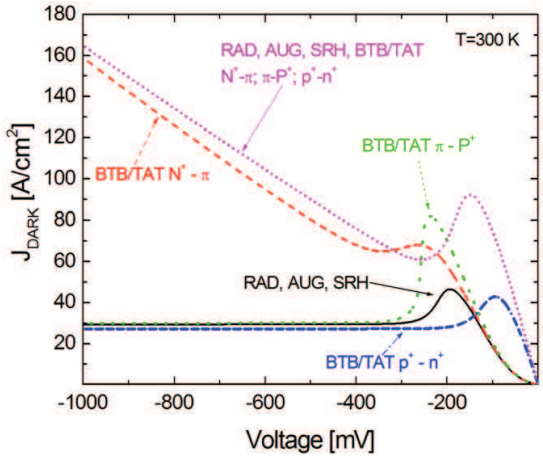


Fig. 7. Contribution of the G-R mechanisms in $J_{DARK}$ voltage characteristics.

The contribution of the G-R mechanisms presented in Fig. 7 is directly connected with both electron and hole concentrations. Carrier concentration profiles of the structure are presented in Fig. 8 (a) and (b) (for $V = -250$ mV corresponding to $\approx J_{Min}$) for RAD, AUG, SRH, BTB/TAT contributions on $N^+$-π, π-$P^+$ and $p^+$-$n^+$ heterojunctions. In the π-type absorber region the electron and hole concentrations are below the intrinsic concentration level ($n_i = 3.6\times10^{16}$ cm$^{-3}$) and the desirable AUG G-R suppression is visible. The hole concentration (majority carriers) drops to the level of acceptor doping, while electron concentration is reduced more rapidly (electrons barely contribute to electric conductivity) resulting in the creation of a nearly depletion region within the absorber layer.

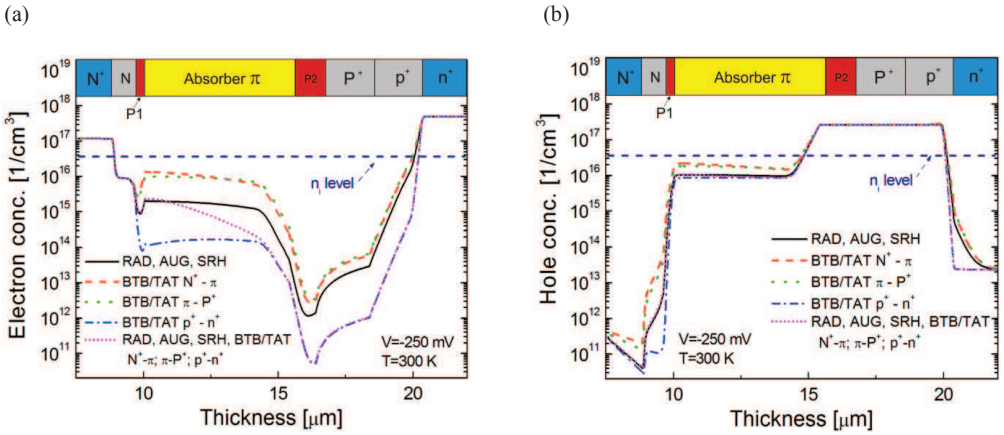


Fig. 8. Electron (a) and hole (b) concentrations in LWIR $N^+/N/P1/\pi/P2/P^+/p^+/n^+$ HgCdTe structure for selected G-R components.

Once the BTB/TAT processes are included in the simulation, tunnelling effects at the $N^+$-π extraction junction increase both electron (nearly five times) and hole ( two times) concentrations in comparison to the RAD, AUG, SRH's contribution (black solid line). Tunnelling effects at the $p^+$-$n^+$ heterojunction reduce both electron and hole concentrations, which in turn, results in a decrease of the carrier concentrations in the absorber region.

P2-$P^+$-$p^+$ barrier's influence on electron transport is also clearly depicted in Fig. 9 (a), where electron current drops (see solid black line) by one order of magnitude in comparison to the $J_{DARK}$ in $N^+$- and $n^+$-contact layers, respectively.

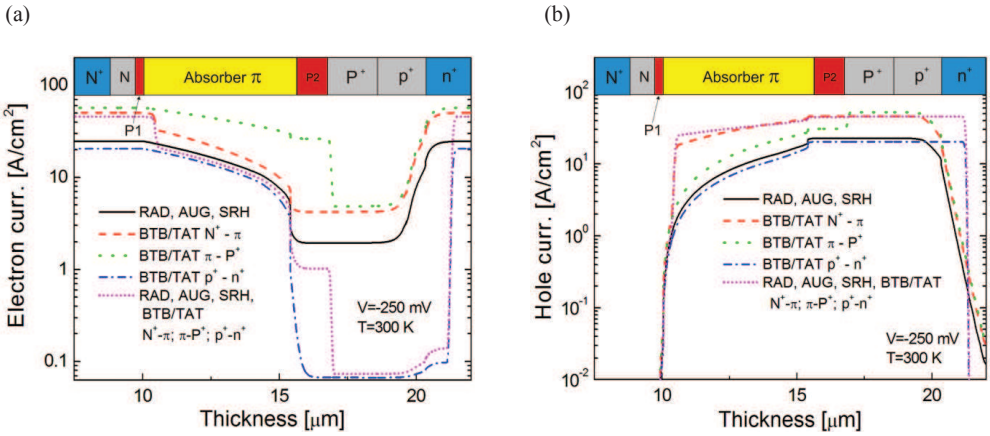


Fig. 9. Electron (a) and hole (b) currents for LWIR $N^+/N/P1/\pi/P2/P^+/p^+/n^+$ HgCdTe structure for selected dark current components.

Since we assumed that BTB/TAT effects dominate in the following regions: 8−10.5 μm ($N^+$-π); 14.5−17 μm (π-$P^+$); 18−21 μm ($p^+$-$n^+$) respectively, we observe a sharp increase of the electron current in the mentioned regions. Similar considerations were performed for hole current versus detectors' profile and the results are presented in Fig. 9 (b).

The dark current and the AUG G-R suppression directly depend on both $N^+$ (contact layer) and $P^+$ (barrier) layers' doping and composition (see Fig. 10). Once the $N^+$-contact layer composition becomes comparable to the π-type absorber, the extraction junction capabilities deteriorate, which in turn leads to dark current's increase. The rise of doping in the $N^+$-contact layer results in higher $J_{DARK}$. The barrier $P^+$ composition influences $J_{DARK}$ for $x < 0.33$ and increases sharply when the analyzed $x$-composition becomes comparable to both the π-type absorber and $n^+$-layer compositions, respectively (exclusion junction capabilities worsen). The optimal doping of barrier depends on applied bias and the lowest $J_{DARK}$ may be achieved for $N_A = 7\times10^{15}$–$6\times10^{16}$ cm$^{-3}$ for analyzed voltages.

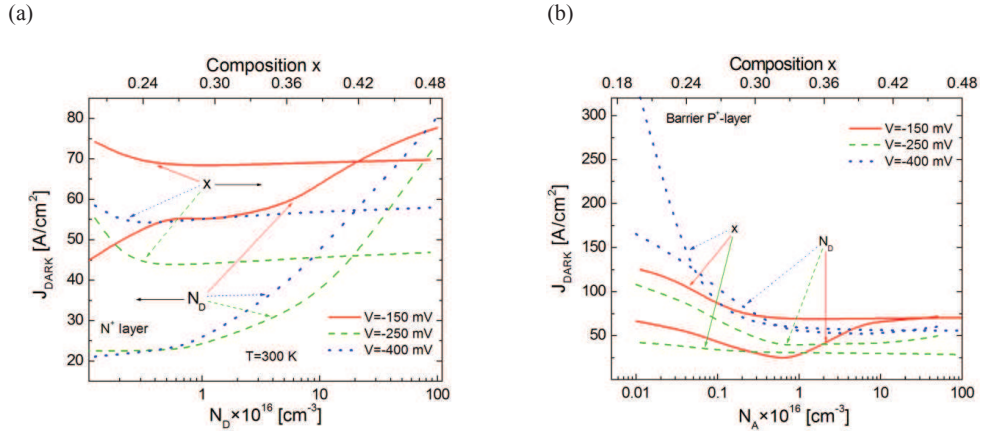


Fig. 10. $J_{DARK}$ of LWIR $N^+$/N/P1/π/P2/$P^+$/$p^+$/$n^+$ HgCdTe versus doping and compositions of $N^+$-contact layer (a) and $P^+$-barrier layer (b).

The influence of $n^+$-layer doping and composition on $J_{Max} - J_{Min}$ is presented in Fig 11 (a). Contact layer composition does not seem to have huge contribution to AUG G-R suppression. The composition increase of $n^+$-contact layer from 0.21 to 0.48 changes $J_{Max} - J_{Min}$ within the range of 30.3−33.5 A/cm$^2$. The maximum value of the Auger G-R reduction is observed for $x = 0.24$.

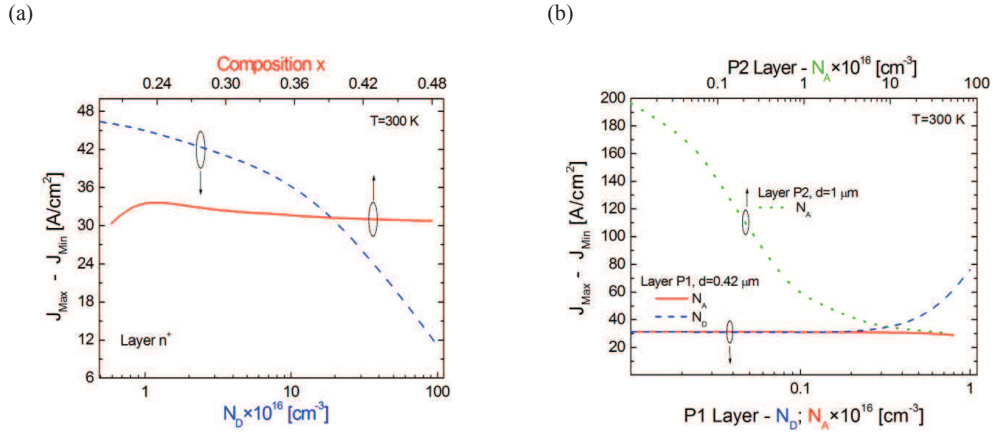


Fig. 11. $J_{Max} - J_{Min}$ for LWIR $N^+$/N/P1/π/P2/$P^+$/$p^+$/$n^+$ HgCdTe versus doping and composition of $n^+$-contact layer (a), and doping of P1, P2 interface layers (b).

The influence of doping of the P1 and P2 $x$-graded interface layers on Auger G-R suppression is depicted in Fig. 11 (b). P1 interface layer was assumed to be both $n$- and $p$-type doped showing

no difference in $J_{Max} - J_{Min}$ to $N_D$, $N_A = 10^{15}$ cm$^{-3}$. Above the $N_D$, $N_A = 10^{15}$ cm$^{-3}$ level, *n*-type doping increases $J_{Max} - J_{Min}$ while *p*-type doping reduces $J_{Max} - J_{Min}$. Considering the *p*-type doped P2 interface layer, $J_{Max} - J_{Min}$ decreases with the doping within the range of $J_{DARK} \approx 200-30$ A/cm$^2$ for the $N_A = 10^{14}-5\times10^{17}$ cm$^{-3}$ range.

### 3.3. Time response and detectivity

The thickness of the π-type absorber layer plays a decisive role in estimation of both $J_{DARK}$ (due to Auger suppression) and optical absorption. These parameters should be taken into consideration in device optimization. As mentioned at the beginning, the absorption coefficient depends on absorber *x*-composition and operating temperature.

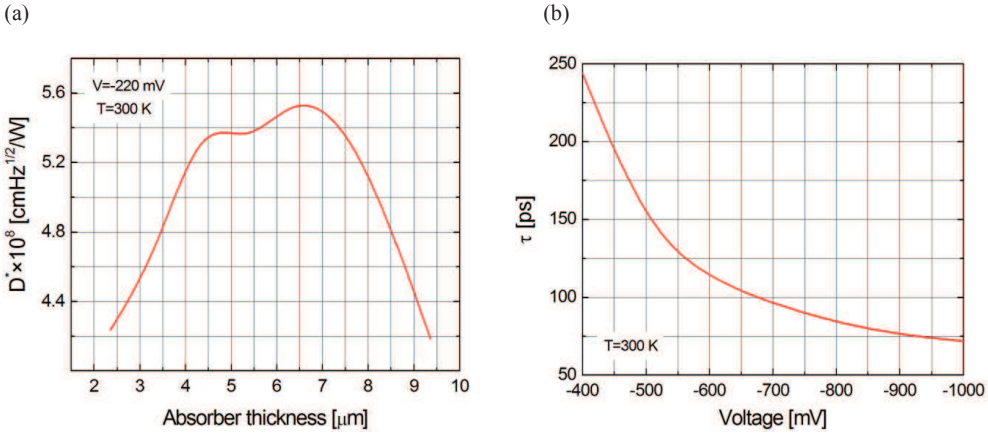


Fig. 12. LWIR $N^+/N/P1/\pi/P2/P^+/p^+/n^+$ HgCdTe structure: (a) detectivity versus absorber thickness (b) response time versus voltage.

Applying reverse bias, it is indispensable to have $N^+$-π (extraction) and π-$P^+$ (exclusion) heterojunctions close enough to keep the carrier concentration below the intrinsic level. On the other hand, if the thickness of the absorber decreases, detectivity decreases due to spectral response reduction (absorption volume drops). $J_{DARK}$ decreases with absorber's layer reduction due to decreasing of the carrier generation rate.

Device optimization should be performed for every single bias condition. Figure 12 (a) presents calculated detectivities versus thickness of the absorber layer. The optimal absorber thickness was estimated to be slightly higher in comparison to the one assumed at the growth process ($d = 5.4$ μm).

Except detectivity, many IR applications require fast response devices (even subnanosecond time constants). According to the experimental data, the measured time constants at $V = -700$ mV and $T = 230$ K are in the range $\tau = 600$ ps, while for the simulated structure it was estimated in the range of $\tau = 90-140$ ps [see Fig. 12 (b)]. Reverse bias in the range of $V = -400$ to $-1000$ mV applied to the simulated structure reduces the time constant nearly four times. This behavior is directly connected with the decrease of carrier concentration in the absorber region resulting in lowering of the G-R rates. Further rapid reduction of the time constant for higher biases is joined with increasing of both the ambipolar mobility and ambipolar diffusion coefficient in π-type absorber due to decreasing of electron concentration in comparison to the acceptor concentration level.

## 4. Comparison to the "Rule 07"

The very last figure (Fig. 13) compares the dark current ($J_{Min}$) of the simulated structure $N^+/N/P1/\pi/P2/P^+/p^+/n^+$ (calculated for two sets of characteristic SRH and TAT lifetimes) to the values given by "Rule 07" (LWIR, $\lambda_c$ = 8.3 μm) being a simple means to compare the HgCdTe IR detectors [43]. It is clearly evident that calculated values for simulated $N^+/N/P1/\pi/P2/P^+/p^+/n^+$ do not surpass the "Rule 07" due to both SRH and TAT mechanisms in the analyzed temperature range. It must be stressed that $J_{Min}$ values were estimated under bias condition. Doping of the $n^+$ contact layer was assumed to be $N_D = 5\times10^{17}$ cm$^{-3}$.

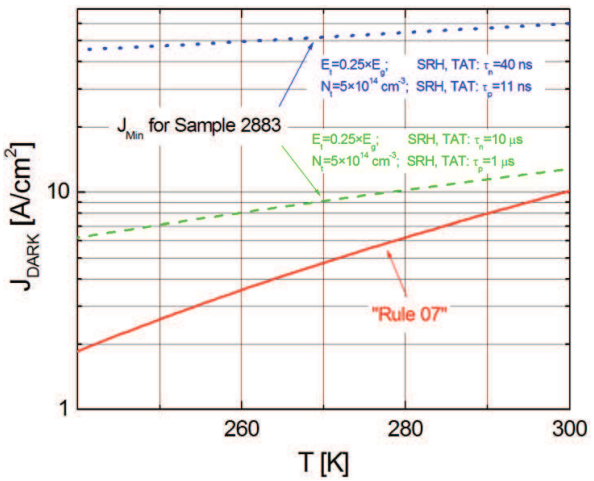


Fig. 13. Comparison of dark currents for LWIR $N^+/N/P1/\pi/P2/P^+/p^+/n^+$ HgCdTe structure and estimated after "Rule 07".

## 5. Conclusions

In the paper we estimated and compared with experimental results the performance of the LWIR HgCdTe $N^+/N/P1/\pi/P2/P^+/p^+/n^+$ AUG G-R suppressed detector designed for HOT conditions. It was shown that electron concentration in the absorber region is reduced by one order of magnitude in comparison to the intrinsic level fully proving the AUG G-R suppression. Dark current was analyzed in detail as a function of the structural parameters, in particular $N^+$-, $n^+$-contacts and P1-, P2-interfaces and $P^+$-barrier layers, respectively. The optimized structural parameters were presented for selected voltages.

Presented time constants are in the range of 100 ps for high voltages, while detectivities could be easily increased by incorporation of immersion (e.g. GaAs lens) to ≈ $10^{10}$ cmHz$^{1/2}$/W at $T$ = 300 K. It was shown that proper optimization of the $N^+$-π (extraction), π-$P^+$ (exclusion) and $p^+$-$n^+$ heterojunctions easily allows controlling of the AUG G-R rate in the detector's structure.

## Acknowledgements

This paper has been done under financial support of the Polish National Science Centre, Project: DEC 2011/01/B/ST5/06283.

## References


[1] Rogalski A. (2011). *Infrared Detectors,* second edition. CRC Press, Boca Raton.

[2] Martyniuk P., Rogalski A. (2013). HOT infrared detectors. *Opto-Electron. Rev*., 21(2), 239–257.

[3] Rogalski A. (2005). HgCdTe infrared detector material: history, status and outlook. *Rep. Prog. Phys.*, 68, 2267–2336.

[4] Norton P. (2002). HgCdTe infrared detectors. *Opto-Electron. Rev.*, 10, 159–174.

[5] Piotrowski J., Rogalski A. (2007). *High-Operating-Temperature Infrared Photodetectors*. Ed. SPIE, Bellingham, ISBN: 9780819465351.

[6] Piotrowski J. and Piotrowski A. (2011). *Room temperature photodetectors*. Mercury Cadmium Telluride: Growth, Properties and Applications edited by Peter Capper and James Garland, Willey, 513–537.

[7] Piotrowski J. (1972). A new method of obtaining CdHgTe thin films. *Electr. Technol*., 5, 87–89.

[8] Jezykowski R., Persak T., Piotrowski J. (1972). Uncooled photodetectors based on 8-12 μm HgCdTe layers. (in Polish), *Biul. WAT*, 5, 105–109.

[9] Grudzien M. and Piotrowski J. (1989). Monolithic optically immersed HgCdTe IR detectors. *Infrared Phys*., 29, 251–253.

[10] Ashley T. and Elliott C. T. (1985). Non-equilibrium mode of operation for infrared detection. *Electron. Lett.*, 21, 451–452.

[11] Ashley T. and Elliott C. T. (1991). Operation and properties of narrow-gap semiconductor devices near room temperature using non-equilibrium techniques. *Semicond. Sci. Technol.*, 6, C99–C105.

[12] Ashby M. K., Gordon N. T., Elliott C.T., Jones C.L., Maxey C. D., Hipwood L. and Catchpole R. (2003). Novel $Hg_{1-x}Cd_xTe$ device structure for higher operating temperature detectors. *J. Electron. Mat*. 32, 667–671.

[13] Maxey C.D., Jones C.L., Metcalfe N.E., Catchpole R.A., Gordon N.T., White A.M. and Elliot C.T. (2007). MOVPE growth of improved non-equlibrium MCT device structures for near ambient temperature heterodyne detectors. *Proc. SPIE*, 3122, 453–464.

[14] Adamiec K., Gawron W., Piotrowski J. (1997). Isothermal vapor phase epitaxy and RF sputtering for band gap engineered HgCdTe. *Proc. SPIE*, 3179, 251–255.

[15] Piotrowski J., Grudzień M., Nowak Z., Orman Z., Pawluczyk J., Romanis M. and Gawron W. (2000). Uncooled photovoltaic $Hg_{1-x}Cd_xTe$ LWIR detectors. *Proc. SPIE*, 4130, 175–184.

[16] Wenus J., Rutkowski J., Rogalski A. (2001). Two-Dimensional Analysis of Double-Layer Heterojunction HgCdTe Photodiodes. *IEEE Transactions on Electron Devices*, 48, 1326–1332.

[17] Rutkowski J., Wenus J. (2001). Inherent and additional limitations of HgCdTe heterojunction photodiodes. *Opto-Electron. Rev*., 9, 331–335.

[18] Wenus J., Rutkowski J., (2002). Influence of valence-band barriers in VLWIR HgCdTe P-on-n heterojunctions on photodiode parameters. *Phys. Stat. Sol. (b)*, 229, 1093–1096.

[19] Kubiak L., Madejczyk P., Wenus J., Gawron W., Jóźwikowski K., Rutkowski J., Rogalski A. (2003). Status of HgCdTe photodiodes at the Military University of Technology. *Opto-Electron. Rev.*, 11, 211–226.

[20] Piotrowski J., Gawron W., Orman Z., Pawluczyk J., Kłos K., Stępień D. and Piotrowski A. (2010). Dark currents, responsivity, and response time in graded gap HgCdTe structures. *Proc. SPIE*, 7660, 766031-766031-8.

[21] Klipstein P. (2008). XBn' barrier photodetectors for high sensitivity and high operating temperature infrared sensors. *Proc. SPIE*, 6940, 69402U-1–11.

[22] Ting D. Z., Hill C. J., Soibel A., Nguyen J., Keo S., Lee M. C., Mumolo J. M., Liu J. K., and Gunapala S. D. (2010). Antimonide-based barrier infrared detectors. *Proc. SPIE*, 7660, 76601R.

[23] Ting D. Z., Soibel A., Höglund L., Nguyen J., Hill C.J., Khoshakhlagh A., and Gunapala S. D. (2011). Type-II superlattice infrared detectors. In *Semiconductors and Semimetals*, edited by S. D. Gunapala, D. R. Rhiger, and C. Jagadish, Elsevier, Amsterdam.

[24] Rogalski A., Martyniuk P. (2006). InAs/GaInSb superlattices as a promising material system for third generation infrared detectors. *Infrared Physics & Technol.*, 48, 39–52.

[25] Martyniuk P., Rogalski A. (2008). Comparison of performance of quantum dot and other types infrared photodetectors. *Proc. SPIE*, 6940, 694004.

[26] Martyniuk P., Wrobel J., Plis E., Madejczyk P., Kowalewski A., Gawron W., Krishna S., Rogalski A. (2012). Performance modeling of MWIR InAs/GaSb/B-$Al_{0.2}Ga_{0.8}Sb$ type-II superlattice nBn detector. *Semicond. Sci. Technol.*, 27, 055002.

[27] Wróbel J., Martyniuk P., Plis E., Madejczyk P., Gawron W., Krishna S., Rogalski A. (2012) Dark current modeling of MWIR type-II superlattice detectors. *Proc. SPIE*, 8353, 8353-16.

[28] Martyniuk P., Wróbel J., Plis E., Madejczyk P., Gawron W., Kowalewski A., Krishna S., Rogalski A. (2013). Modeling of mid wavelength infrared InAs/GaSb type II superlattice detectors. *Optical Engineering* **52**, 061307-1–12.

[29] Gawron W., Piotrowski J. (1994). Practical near room-temperature, long-wavelength IR photovoltaic detectors. *Opto-Electron. Rev*., 2, 91–94.

[30] Piotrowski J., Gawron W. (1995). Extension of longwavelength IR photovoltaic detector operation to near room-temperatures. *Infrared Physics & Technol.*, 36, 1045-1051.

[31] Piotrowski J., Gawron W. (1997). Ultimate performance of infrared photodetectors and figure of merit of detector material. *Infrared Physics & Technol.*, 38, 63-68.

[32] *www.vigo.com.pl*

[33] Piotrowski A., Piotrowski J., Gawron W., Pawluczyk J., Pedzinska M. (2009). Extension of usable spectral range of Peltier cooled photodetectors. *Acta Physica Polonica A*, 116, 52–55.

[34] Piotrowski A., Piotrowski J., Gawron W., Pawluczyk J., Pedzinska M. (2009). Extension of spectral range of Peltier cooled photodetectors to 16 μm. *Proc. SPIE*, 7298, 729824.

[35] Stanaszek D., Piotrowski J., Piotrowski A., Gawron W., Orman Z., Paliwoda R., Brudnowski M., Pawluczyk J. , Pedzińska M. (2009). Mid and long infrared detection modules for picosecond range measurements. *Proc. SPIE*, 7482, 74820M-74820M-11.

[36] Piotrowski J., Pawluczyk J., Piotrowski A., Gawron W., Romanis M., Kłos K. (2010). Uncooled MWIR and LWIR photodetectors in Poland. *Opto-Electron. Rev*., 18, 318–327.

[37] APSYS Macro/User's Manual ver. 2011. (2011). Crosslight Software, Inc.

[38] Martyniuk P., Rogalski A. (2013). Modeling of MWIR HgCdTe complementary barrier HOT detector. *Solid-State Electronics*, 80, 96–104.

[39] Martyniuk P., Rogalski A. (2013). Theoretical modeling of MWIR thermoelectrically cooled nBn HgCdTe detector. *Bull. Pol. Ac.: Tech.,* 61, 1.

[40] Capper P. P. (1994). *Properties of Narrow Gap Cadmium-based Compounds*, London, U.K.: Inst. Elect. Eng.

[41] Piotrowski A., Madejczyk P., Gawron W., Kłos K. Pawluczyk J., Rutkowski J., Piotrowski J., Rogalski A. (2007). Progress in MOCVD growth of HgCdTe heterostructures for uncooled infrared photodetectors. *Infrared Physics & Technol.* 49, 173–182.

[42] Madejczyk P., Piotrowski A, Kłos A., Gawron W., Rutkowski J., Rogalski A. (2010). Control of acceptor doping in MOCVD HgCdTe epilayers. *Opto-Electron. Rev.*, 18, 271–276.

[43] Tennant W. E., Lee D., Zandian M., PiQuette E., Carmody M. (2008). MBE HgCdTe Technology: A very general solution to IR detection, described by „Rule07", a very convenient heuristic. *J. Electron. Mater.*, 37, 1406–1410.